

Measurement of the $E_r^{c.m.} = 138$ keV resonance in the $^{23}\text{Na}(p,\gamma)^{24}\text{Mg}$ reaction and the abundance of sodium in AGB stars

J. M. Cesaratto,* A. E. Champagne, M. Q. Buckner, T. B. Clegg, S. Daigle, C. Howard, C. Iliadis, R. Longland, J. R. Newton, and B. M. Oginni

University of North Carolina at Chapel Hill, Chapel Hill, North Carolina 27599-3255, USA
and Triangle Universities Nuclear Laboratory, Durham, North Carolina 27708-0308, USA

(Received 26 September 2013; published 18 December 2013)

Globular clusters represent some of the oldest stellar aggregations in the universe. As such, they are used as testing grounds for theories of stellar evolution and nucleosynthesis. Astronomical observations have shown star-to-star abundance variations in light-mass elements in all galactic globular clusters that are not predicted by standard stellar evolution models. In particular, there exists a pronounced anticorrelation between Na and O in the cluster stars that is not observed in field stars of similar evolutionary state. The abundance of Na is regulated in part by the $^{23}\text{Na}+p$ reaction, which is also a bridge between the NeNa and the MgAl mass regions, but the $^{23}\text{Na}(p,\gamma)^{24}\text{Mg}$ reaction rate is very uncertain for burning temperatures relevant to stars on the red giant and asymptotic giant branches. This uncertainty arises from an expected but unobserved resonance at $E_r^{c.m.} = 138$ keV. The resonance strength upper limit has been determined to be $\omega\gamma_{UL}(138 \text{ keV}) \leq 5.17 \times 10^{-9}$ eV with indications of a signal at the 90% confidence level. New reaction rates have been calculated for the $^{23}\text{Na}(p,\gamma)^{24}\text{Mg}$ and $^{23}\text{Na}(p,\alpha)^{20}\text{Ne}$ reactions and the recommended value for the $^{23}\text{Na}(p,\gamma)^{24}\text{Mg}$ rate has been reduced by over an order of magnitude at $T_9 = 0.07$. This will have implications for the processing of material between the NeNa and MgAl mass regions.

DOI: 10.1103/PhysRevC.88.065806

PACS number(s): 25.40.Lw, 26.20.Cd, 27.30.+t

I. INTRODUCTION

The globular clusters in the halo of our galaxy are the oldest galactic objects for which reliable ages have been determined and are thought to be the first structures to form in the early history of the galaxy. Thus, they provide information about the early galaxy and place a lower limit on the age of the universe.

To first order, clusters are coeval groups of stars, formed from a homogeneous reservoir of primordial gas. However, observations paint a more complicated and dynamic picture. Although most clusters have the same metallicity to within a narrow range, every well-studied globular cluster shows star-to-star abundance variations for light elements (C, N, O, Na, Mg, and Al) with correlations between Na and Al and O-Na and Mg-Al anticorrelations (see Ref. [1] for a review). The source(s) of these anomalous variations is currently uncertain, but these effects are seen in main sequence and subgiant stars that are not hot enough to produce them *in situ* [2]. This implies that gas, which was similar in composition to what is observed in field halo stars, was contaminated with gas that had been processed and ejected from a previous generation of stars and, thus, the abundance anomalies contain information about the early history of the cluster. Although no models can account for the observations in detail, possible progenitor sources include massive asymptotic giant branch (AGB) stars [3–5], rotating, massive AGBs [6], rotating massive stars [7,8], and massive

binaries [9]. In addition, nonstandard mixing may be needed to explain the observed oxygen abundances [10] as well as the O-Na anticorrelation [11].

The observations also show that Na/Fe can be enhanced with respect to the solar ratio, which suggests nuclear processing of stellar material beyond the CNO cycle, i.e., in the NeNa and MgAl chains. The $^{23}\text{Na}+p$ reaction plays a central role in the O-Na anticorrelation because it destroys ^{23}Na and the $(p,\alpha)/(p,\gamma)$ branching ratio determines how much material is recycled in the NeNa mass range and how much is transformed to the MgAl mass range [12]. The relevant reaction flow is shown in Fig. 1.

The existing reaction rate for $^{23}\text{Na}(p,\gamma)^{24}\text{Mg}$ ($Q_{p\gamma} = 11692.68(01)$ keV [13]) is most uncertain for the burning temperatures $T = 0.04\text{--}0.15$ GK ($T_9 = 0.04\text{--}0.15$), where the dominant contributions to the reaction process are from direct capture and low-energy, narrow resonances. Figure 2 shows a simplified level scheme of ^{24}Mg [14,15]. Direct measurements of the $^{23}\text{Na}+p$ system extend down to the $E_r^{c.m.} = 170$ -keV resonance in the $^{23}\text{Na}(p,\alpha)^{20}\text{Ne}$ reaction [16,17]. The strength of this resonance in the (p,γ) channel is 10^4 times smaller than that of the (p,α) channel and thus it is not a significant contributor to the $^{23}\text{Na}(p,\gamma)^{24}\text{Mg}$ rate. Below $E_r^{c.m.} = 170$ keV there are four states that could correspond to resonances at $E_r^{c.m.} = 5, 37, 138,$ and 167 keV. The 167-keV resonance has high spin, $J^\pi \geq 6^+$, and is thus not astrophysically significant. Görres *et al.* [17] set an upper limit on the resonance strength for the 138-keV resonance in the (p,γ) channel, $\omega\gamma_{p\gamma} \leq 5 \times 10^{-6}$ eV. Indirect measurements of these states via $^{23}\text{Na}(^3\text{He},d)^{24}\text{Mg}$ by Hale *et al.* [15], showed that the 5- and 37-keV resonances made negligible contributions to the total reaction rate. They observed a state at

*Current address: SLAC National Accelerator Laboratory, 2575 Sand Hill Rd., MS 54, Menlo Park, CA, 94025, USA; cesaratto@stanford.edu

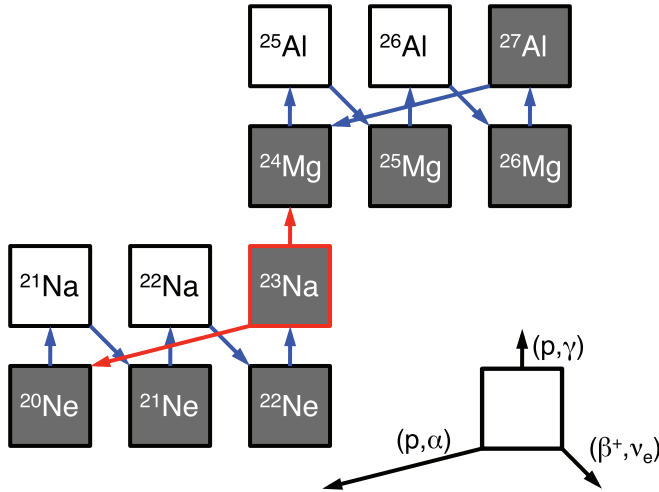


FIG. 1. (Color online) The reactions in the NeNa and MgAl regions as they operate in red-giant and AGB stars. The branching at ^{23}Na is highlighted. Stable nuclei are shown in gray.

an excitation energy $E_x = 11831$ keV, that could correspond to the 138-keV resonance (Fig. 6 in Ref. [15]), but distorted-wave Born approximation (DWBA) fits to the data were unable to identify a unique proton orbital angular momentum transfer, l_p , for the reaction. Their 68% confidence-limit (CL) estimates for the resonance strength were based on possible l_p transfers that were consistent with the deuteron angular distribution, which are listed in Table I. From these estimates, it was concluded that this resonance could be astrophysically significant for $l_p < 3$. A direct search by Rowland *et al.* [12] did not result in a detection but produced a reduced upper limit on the resonance strength,

TABLE I. Estimated resonance strengths for the $E_r^{\text{c.m.}} = 138$ keV resonance with 68% confidence intervals [15].

l_p	$\omega\gamma$ (eV)
0	$5.4\text{--}14 \times 10^{-6}$
1	$2.6\text{--}6.6 \times 10^{-7}$
2	$0.9\text{--}2.4 \times 10^{-8}$
3	$1.8\text{--}4.6 \times 10^{-10}$

$\omega\gamma_{p\gamma}(138 \text{ keV}) \leq 1.5 \times 10^{-7}$ eV, which would exclude the possibly of $l_p = 0$ (*s*-wave) transfer.

More recently, Iliadis *et al.* [18] computed the $^{23}\text{Na}(p,\gamma)^{24}\text{Mg}$ reaction rate using a new Monte Carlo method [19]. All experimental input to date was included and large uncertainties were found to exist for $T_9 = 0.04\text{--}0.15$ because of the unobserved 138-keV resonance. At key burning temperatures for hot bottom burning in AGB stars, $T_9 \sim 0.07\text{--}0.08$, the uncertainty is a factor of 28 (68% confidence interval). These large uncertainties are a limiting factor in the predictions of ^{23}Na abundances in stellar models. Thus, the aim here is to further reduce this uncertainty by again directly searching for the 138-keV resonance using an improved experimental setup.

II. EXPERIMENTAL PROCEDURE

A. Accelerators

We measured the $^{23}\text{Na}(p,\gamma)^{24}\text{Mg}$ reaction at the Laboratory for Experimental Nuclear Astrophysics (LENA), located at the Triangle Universities Nuclear Laboratory. The sensitivity of the most recent search for the 138-keV resonance [12] (also at LENA) was limited by the amount of beam available. To improve on this situation, we have constructed a new high-intensity, low-energy accelerator based on an electron cyclotron resonance ion source (ECRIS) [20]. The ECRIS uses permanent magnets to establish the axial, magnetic field (0.0875 mT for microwave power at 2.45 GHz) and is mounted on a 0-200 kV platform. Typical beam currents on target were in excess of 1 mA. The energy resolution of the beam was <800 eV and the energy of the beam was calibrated to better than 500 eV using the $E_r^{\text{lab}} = 150.82(9)$ -keV resonance in $^{18}\text{O}(p,\gamma)^{19}\text{F}$ ($Q_{p\gamma} = 7994.8(6)$ keV [13], $\Gamma \leq 0.3$ keV [21]) and the $E_r^{\text{lab}} = 202.8(9)$ -keV [14] resonance in $^{27}\text{Al}(p,\gamma)^{28}\text{Si}$ ($Q_{p\gamma} = 11585.11(12)$ keV [13]).

A 1-MV model JN Van de Graaff accelerator was used to provide beam for diagnostic purposes and testing of target uniformity and stability. Proton beams of up to 550 keV were accelerated with intensities of $25 \mu\text{A}$ and typical energy spread of less than 1 keV. The energy calibration was established to <1 keV by using well-known resonances of the reactions $^{18}\text{O}(p,\gamma)^{19}\text{F}$, $^{26}\text{Mg}(p,\gamma)^{27}\text{Al}$, and $^{27}\text{Al}(p,\gamma)^{28}\text{Si}$.

B. Targets

Previous measurements of the $^{23}\text{Na}(p,\gamma)^{24}\text{Mg}$ reaction have used targets of NaCl and Na_2WO_4 evaporated onto thin metal sheets. However, we initially investigated implanted targets, which are clean, isotopically pure (though that is not

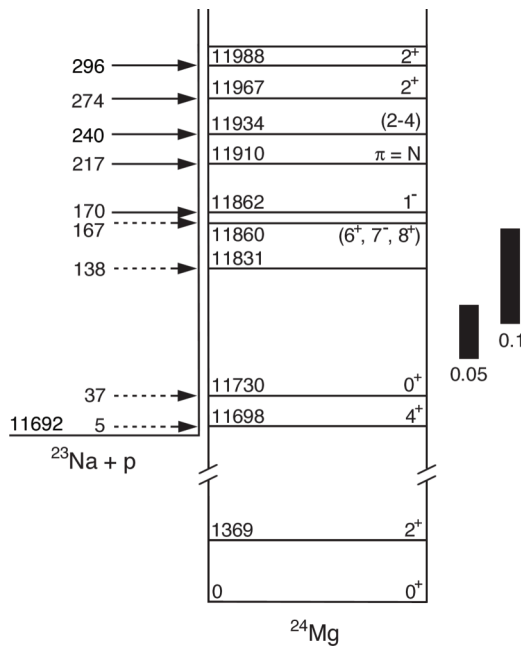


FIG. 2. Energy level diagram of ^{24}Mg [14,15]. All energies (keV) are represented in the center-of-mass frame. The Gamow windows are listed at the right for $T_9 = 0.05$ and 0.1 .

an issue for ^{23}Na targets) and have been shown to be relatively stable under high beam loads. Previous attempts by Seuthe *et al.* [22] showed success in implanting ^{23}Na into nickel, but we were unable to reproduce these results [23]. Ultimately, targets were produced by evaporating Na_2WO_4 onto $38 \times 38 \times 0.3$ -mm thick tantalum backings. The backings were fabricated from high-purity (99.993%) tantalum that was wet-acid etched in a chemical bath according to the procedure in Ref. [24] in order to remove surface impurities. After etching, the backings were resistively heated in a vacuum of ≤ 1 μTorr to further drive impurities from the surface. Samples of Na_2WO_4 were purchased from five companies and were assayed through in-beam measurement to determine which contained the least amount of contamination. For the energy region we probed, $E_p^{\text{lab}} \approx 150$ keV, problematic contaminants occur from the broad resonance in $^{11}\text{B}(p,\gamma)^{12}\text{C}$ at $E_r^{\text{lab}} = 167$ keV and from direct capture in the $^2\text{H}(p,\gamma)^3\text{He}$ and $^{12}\text{C}(p,\gamma)^{13}\text{N}$ reactions. The in-beam measurements showed that the Na_2WO_4 compound produced by Cerac, Inc. contained the least amount of ^{11}B , so it was used to produce all of the targets used for data acquisition. Deuterium contamination was traced to the use of oil-based mechanical pumps and so the targets were produced using an evaporator with an oil-free pumping system.

Since low-energy resonances in the $^{23}\text{Na}(p,\gamma)^{24}\text{Mg}$ reaction are separated by several tens of keV, the targets had thicknesses on the order of $\Delta E = 50$ keV at a proton bombarding energy of 150 keV. Tests of stability under high beam loads showed that the maximum yield remained constant during beam bombardment, but the target thickness was reduced by approximately 1–2 keV/C at $E_p^{\text{lab}} = 150$ keV and a beam current of 1000 μA . Targets were replaced once their thickness was reduced to $\Delta E = 10$ –15 keV. The beam entered the target chamber through a copper tube, extending to less than 1 cm from the surface of the target. The copper tube was cooled by a LN_2 reservoir to trap potential target contaminants. In order to suppress the emission of secondary electrons from the target, permanent magnets were located at the end of the tube along with an electrode biased to -300 V. To minimize degradation of the targets from beam heating, they were cooled using chilled, deionized water.

The expected stoichiometry of the evaporated targets ($N_{\text{Na}}:N_{\text{W}}:N_{\text{O}} = 2:1:4$) was checked by measuring the excitation function (yield curve) of the $E_r^{\text{lab}} = 512$ keV resonance in $^{23}\text{Na}(p,\gamma)^{24}\text{Mg}$ ($\Gamma < 50$ eV [14], $\omega\gamma = 91.3(125)$ meV [25]). The primary transition to the first-excited state of ^{24}Mg ($R \rightarrow 1$, $E_\gamma = 10619.8$ keV) was measured at 0° with respect to the direction of the beam. The angular distribution coefficient in this geometry was $W(0^\circ) = 0.993$ [26]. Each data point was corrected for coincident summing and the measured yield curve was fit via a Markov-chain Monte Carlo method [27] using the analytical expression in Ref. [28]. In this manner, the maximum yield, the area under the yield curve, the target thickness, and the beam energy resolution were extracted. The first three parameters are needed for calculating the resonance strength. Figure 3 shows a yield curve with a corresponding fit. Assuming $N_{\text{Na}}:N_{\text{W}}:N_{\text{O}} = 2:1:4$, the resonance strength deter-

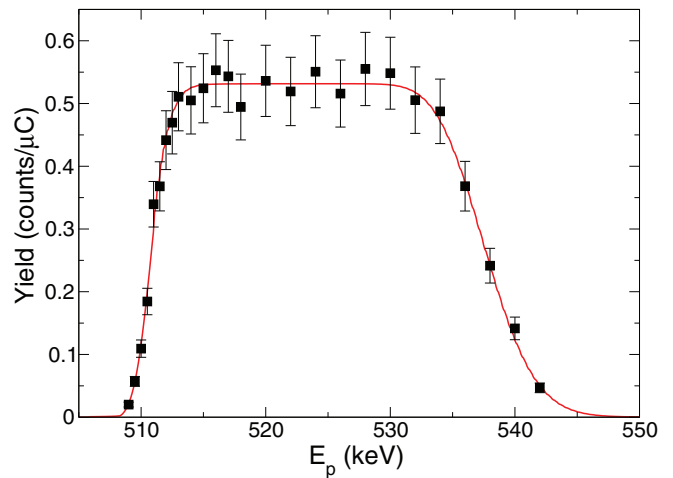


FIG. 3. (Color online) Measured yield curve for the the $E_r^{\text{lab}} = 512$ keV resonance in $^{23}\text{Na}(p,\gamma)^{24}\text{Mg}$ using a Na_2WO_4 target. The data show the γ -ray yield at $E_\gamma = 10619.8$ keV from the $R \rightarrow 1$ transition in ^{24}Mg . These data were corrected for coincident summing and fit using a Markov-chain Monte Carlo method.

mined using the area under the yield curve and the target thickness was $\omega\gamma_{p\gamma} = 88.5 \pm 9.2$ meV, which is in excellent agreement with the literature value, $\omega\gamma = 91.3(125)$ meV [25]). Thus, a stoichiometry of $N_{\text{Na}}:N_{\text{W}}:N_{\text{O}} = 2:1:4$ was adopted. Subsequent measurements of target stability showed that this stoichiometry remained constant under high beam load.

C. Detectors

The target was viewed by a 135% coaxial HPGe detector, 89.0 ± 0.5 mm in diameter, and 91.6 ± 1.0 mm in length [29,30]. It was centered axially on the beam line at 0° with respect to the target chamber at a distance of 1.6 cm, measured from the front of the target to the front of the detector face. The HPGe and target chamber were surrounded by an annulus of NaI(Tl) scintillators. The entire annulus had dimensions 33.0 cm length, 35.7 cm outer diameter, and 11.8 cm inner diameter and was centered axially on the target. Since states in ^{24}Mg in the vicinity of the state of interest decay primarily via γ -ray cascades, the HPGe and NaI(Tl) detectors were operated in coincidence, which significantly reduced low-energy environmental backgrounds. The HPGe and NaI(Tl) detectors were surrounded on all sides by a 12.7-mm thickness of lead, which was in turn encased on all sides (except for the bottom) by 50-mm-thick plastic scintillating paddles [29], used as a veto for cosmic-ray-induced muons.

1. HPGe

Efficiency measurements for γ -ray energies below 3 MeV for the HPGe detector were made by using radioactive sources, ^{22}Na , ^{54}Mn , ^{56}Co , ^{60}Co , and ^{137}Cs . For γ -ray energies above 3 MeV, the nuclear reactions $^{14}\text{N}(p,\gamma)^{15}\text{O}$, $^{27}\text{Al}(p,\gamma)^{28}\text{Si}$, and $^{23}\text{Na}(p,\gamma)^{24}\text{Mg}$ were measured. The data for all sources and reactions emitting more than one γ ray were corrected for coincident summing. To remove any reliance on knowledge

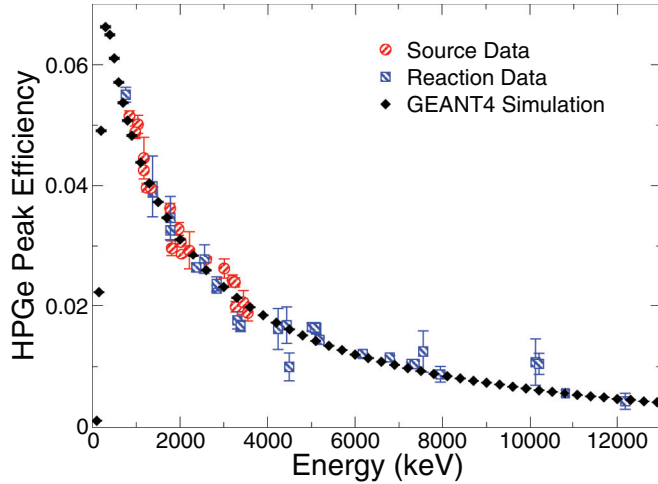


FIG. 4. (Color online) Full-energy peak efficiencies for the HPGe detector. All source and reaction data, and the GEANT4 simulation, have been normalized to the absolute efficiency determined by the sum-peak method [31] using ^{60}Co .

of the activities of the various sources, the *sum-peak method* [31], utilizing ^{60}Co , was used to obtain an absolute efficiency to which the other source and reaction data could be normalized. Monte Carlo calculations with GEANT4 [32] were performed for the energy range, $E_\gamma = 0.1\text{--}13$ MeV and were also normalized to the sum-peak efficiency. The measured energy dependence of the efficiency is well reproduced by the calculation, as shown in Fig. 4.

2. NaI(Tl)

Since the Q value of the $^{23}\text{Na}(p,\gamma)^{24}\text{Mg}$ reaction is high (~ 11.7 MeV), it is likely that the decay of a state in this energy region will give rise to a cascade of γ rays as it deexcites to the ground state. Thus, the NaI(Tl) detector was used to detect some fraction of the decay energy associated with the deexcitation of the 11831-keV state in coincidence with the full energy of a characteristic cascade transition (e.g., the $E_\gamma = 1369\text{-keV } 1 \rightarrow 0$ transition), measured in the HPGe detector. Cuts were placed on the total energy deposited, i.e.,

$$E_{\min} < E^{\text{Ge}} + E^{\text{NaI}} < E_{\max}. \quad (1)$$

The requirement of a minimum energy was used to reduce low-energy backgrounds in the HPGe detector. Therefore, total efficiencies for a given energy range, not peak efficiencies, were needed for the NaI(Tl) detector and these were calculated using GEANT4. The gated total efficiency of the NaI(Tl) detector, which depends on the energy cut, is shown in Fig. 5. Clearly, there is a trade-off between efficiency and the range of the energy cut, and thus the overall background reduction at low energies, which will be discussed in more detail below. An illustration of the level of background reduction achieved with a cut on the total energy is shown in Fig. 6.

3. $\gamma\gamma$ -coincidence efficiency

A coincidence efficiency must be calculated in order to convert the yield measured in the coincidence spectrum to the

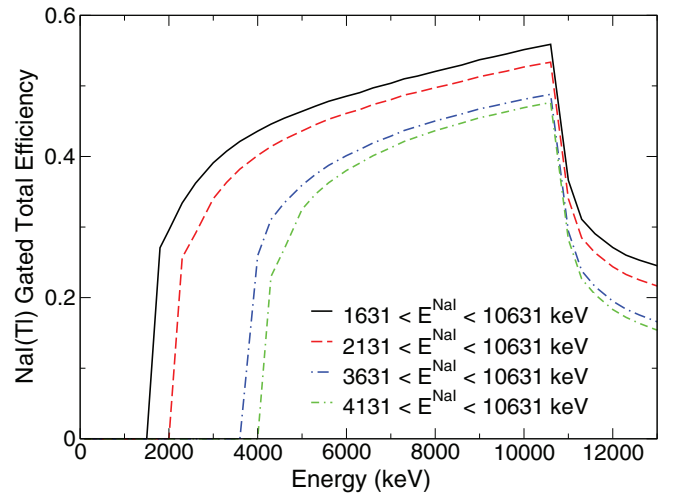


FIG. 5. (Color online) Gated total efficiency for the NaI(Tl) annulus calculated using GEANT4. Each curve represents the total efficiency for a specific energy cut in the NaI(Tl) annulus.

actual number of reactions produced in the target. The total number of fusion reactions created in a singles experiment can be expressed as

$$N = \frac{N_{ij}}{B_{ij}\eta_{ij}^p W_{ij}}, \quad (2)$$

where N_{ij} is the measured intensity, B_{ij} is the branching ratio, η_{ij}^p is the peak detection efficiency, and W_{ij} is the angular correlation for the transition from an initial level i to final level j . When two detectors are involved, $B\eta W$ is replaced by the function $f_\gamma(B,\eta,W)$. An analytical expression for $f_\gamma(B,\eta,W)$ is derived in Ref. [28] and also described in Ref. [33].

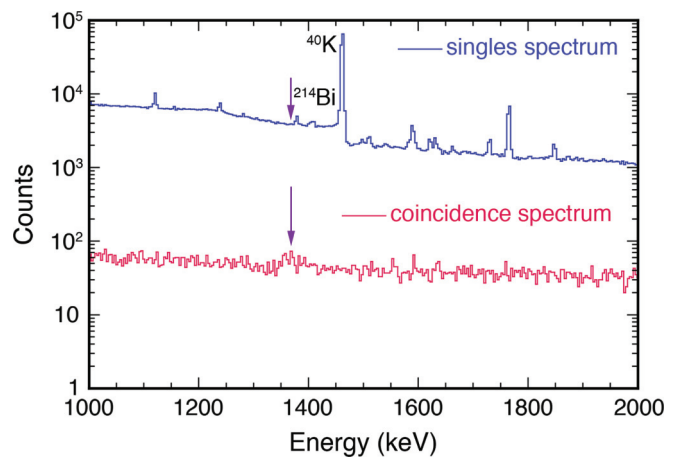


FIG. 6. (Color online) $^{23}\text{Na}(p,\gamma)^{24}\text{Mg}$ HPGe singles spectrum (blue) and HPGe-NaI coincidence spectrum (red). Both spectra were collected with the HPGe detector inside of the NaI annulus and passive shielding. The energy cut on the coincidence spectrum is $3 \text{ MeV} < E^{\text{Ge}} + E^{\text{NaI}} < 12 \text{ MeV}$. The arrows indicate the expected location of the $1369 \text{ keV } \rightarrow 0$ transition in ^{24}Mg .

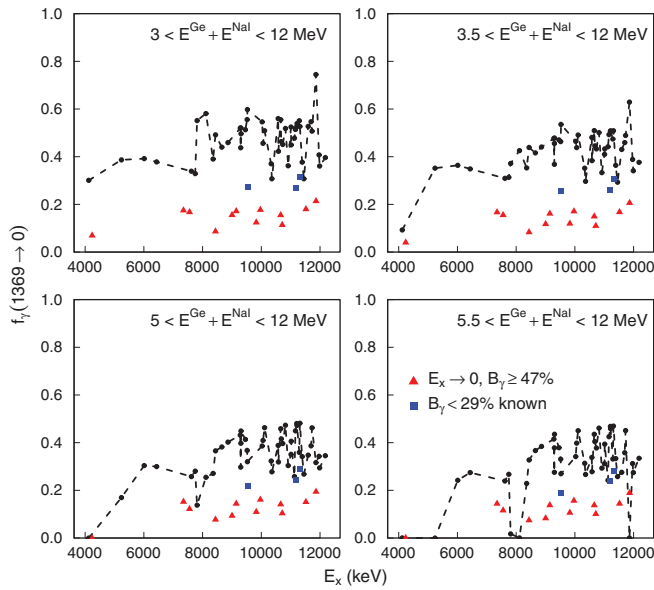


FIG. 7. (Color online) The f_γ calculations for states in ^{24}Mg . For these calculations, the 1369-keV $1 \rightarrow 0$ transition is assumed to be detected in the Ge detector. Each plot corresponds to a calculation with a different lower bound on the energy cut, i.e., $E^{\text{Ge}} + E^{\text{NaI}} = 3, 3.5, 5,$ and 5.5 MeV. All windows have an upper bound of $E^{\text{Ge}} + E^{\text{NaI}} = 12$ MeV.

If the branching of the decay scheme is known for a cascade, then it is possible to couple the branching ratios with the total efficiency of the NaI(Tl) detector to determine an absolute coincidence efficiency. However, in the case of the 11831-keV state in ^{24}Mg , the decay scheme is not known and thus it is necessary to determine an allowable range for f_γ based on the systematics of known decays for nearby states, which allows for an estimate of the coincidence efficiency.

The formalism of Ref. [28] was incorporated into a code, FGAMMA, written in C++, and was further verified through GEANT4 simulations. Branching ratios of 64 levels in ^{24}Mg were included with NaI(Tl) total efficiencies for different energy gates to calculate f_γ for each level. Figure 7 shows the results of the calculations for different NaI(Tl) energy gates with lower bounds $E^{\text{Ge}} + E^{\text{NaI}} > 3, 3.5, 5,$ and 5.5 MeV. All gates have an upper bound of $E^{\text{Ge}} + E^{\text{NaI}} < 12$ MeV to reduce cosmogenic backgrounds. As the energy cut becomes more restrictive, f_γ , and thus the coincidence efficiency, decreases, as indicated in Fig. 7. There, the red triangles correspond to states with greater than 47% primary branch to the ground state and the blue squares are states with less than 29% of the total branching known. The black dashed line through all other states is added simply to guide the eye. Of the states labeled with black circles above 9 MeV, the mean, standard deviation, and minimum values of f_γ are listed in Table II for the different energy gates. Note that γ -ray summing is not considered in the formalism as it is a relatively small correction.

TABLE II. Mean, standard deviation, and minimum f_γ values of states above 9 MeV in ^{24}Mg for detecting a $E_\gamma = 1369$ -keV γ ray in the HPGe detector. The states selected all had ground-state branches of less than 47% of the total decay strength and had at least 27% of the total branching known.

Coincidence gate (MeV) ^a	$f_\gamma(1369 \rightarrow 0)$		
	Mean	St. dev.	Minimum
3–12	0.517	0.097	0.322
3.5–12	0.485	0.087	0.307
5–12	0.379	0.066	0.258
5.5–12	0.348	0.091	0.0

^aFor example, 3–12 MeV refers to $3 \text{ MeV} < E^{\text{Ge}} + E^{\text{NaI}} < 12 \text{ MeV}$.

III. THE MEASUREMENT

A. Observations

On-resonance data were collected using the ECRIS at $E_p^{\text{lab}} = 147.0$ and 148.0 keV. These energies were chosen to be somewhat higher than the expected resonance energy of $E_r^{\text{lab}} = 144.0 \pm 1.5$ keV (calculated using the Q value and excitation energy) so the resonance would be populated within the uniform region of the target. Another consideration in the choice of beam energy was that it had to be below the strong $E_r^{\text{lab}} = 151$ -keV resonance from $^{18}\text{O}(p,\gamma)^{19}\text{F}$, which would arise from the contribution of ^{18}O in the Na_2WO_4 targets. A total of 235.9 C of charge were collected at 148 keV and 11.7 C were collected at 147 keV with an average beam current of $1125 \mu\text{A}$. Nine targets were used for these runs. An additional 141 C of off-resonance data were acquired at $E_p^{\text{lab}} = 138$ keV, using five targets with an average beam current of $1160 \mu\text{A}$. Finally, 11.3 days of data were collected with the beam off in order to measure environmental and cosmic-ray induced backgrounds.

No evidence for a 1369-keV γ ray was observed in the HPGe singles spectrum. However, this line, along with another at 2754 keV (corresponding to the $2 \rightarrow 1$ transition in ^{24}Mg) appeared when a coincidence requirement with the NaI detector was imposed with $3 \text{ MeV} < E^{\text{Ge}} + E^{\text{NaI}} < 12 \text{ MeV}$. These γ rays also appeared in the background spectra and are attributed to the capture of cosmogenic neutrons by ^{23}Na in the NaI detector. The subsequent β^- decay of ^{24}Na ($T_{1/2} = 14.997(12)$ h, $Q_{\beta^-} = 5515.45(8)$ MeV [34]) primarily populates the $E_x = 4123$ keV second-excited state of ^{24}Mg , which decays via a cascade through the first excited state, resulting in the two γ rays that were observed. However, since the Q value for this decay is known, it was possible to remove this contribution from the coincidence spectrum by placing a more restrictive lower bound on the two-dimensional coincidence energy gate. It was found that a requirement of $5 \text{ MeV} < E^{\text{Ge}} + E^{\text{NaI}} < 12 \text{ MeV}$ was sufficient to reduce the contribution of ^{24}Na to a negligible level.

Spectra in the energy region of the 1369-keV $1 \rightarrow 0$ transition in ^{24}Mg for the on-resonance, off-resonance, and background runs with selected coincidence cuts are shown in Figs. 8, 9, and 10, respectively. In these figures, the

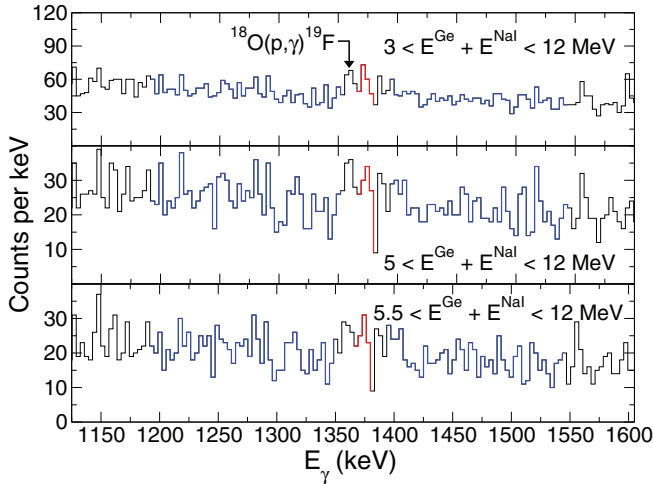


FIG. 8. (Color online) On-resonance coincidence spectra for 3, 5, and 5.5 MeV $< E^{\text{Ge}} + E^{\text{NaI}} < 12$ MeV energy cuts. The regions in red (blue) correspond to the signal (background) region(s) selected for analysis. The top panel shows evidence for a 1369-keV γ ray, but at least some of this strength is the result of the β^- -delayed γ decay of ^{24}Na , caused by capture of cosmogenic neutrons in the NaI detector. There is also evidence for a 1357-keV γ ray arising from the beam-induced contaminant reaction, $^{18}\text{O}(p,\gamma)^{19}\text{F}$.

off-resonance spectra have been normalized to the on-resonance accumulated charge of 247.6 C, while the background spectra have been normalized to the total run time of the on-resonance data, $\tau = 61.15$ h. The regions in red (blue) correspond to the signal (background) region selected for analysis and were the same in all spectra. The on-resonance spectrum in Fig. 8 shows evidence for a 1357-keV γ ray, which can be associated with a beam-induced background contribution from the $^{18}\text{O}(p,\gamma)^{19}\text{F}$ reaction.

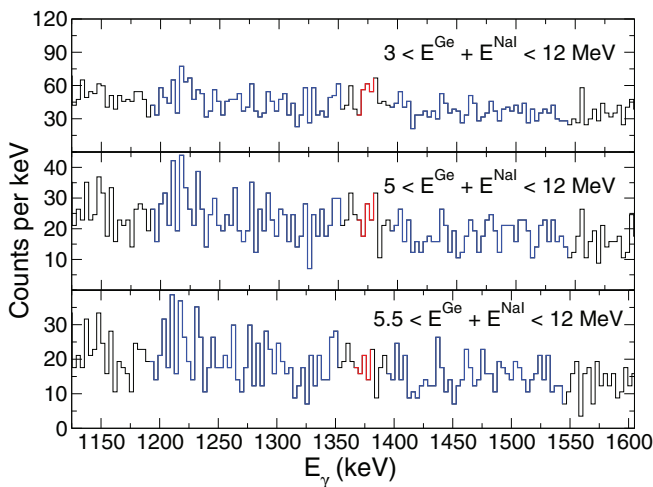


FIG. 9. (Color online) Off-resonance coincidence spectra for 3, 5, and 5.5 MeV $< E^{\text{Ge}} + E^{\text{NaI}} < 12$ MeV energy gates. The spectra have been normalized to the on-resonance accumulated charge of 247.6 C. The regions in red (blue) correspond to the signal (background) region(s) selected for analysis.

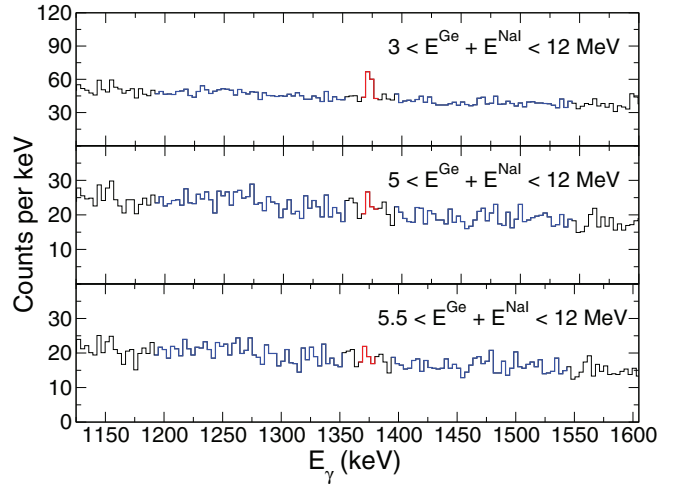


FIG. 10. (Color online) Background coincidence spectra for 3, 5, and 5.5 MeV $< E^{\text{Ge}} + E^{\text{NaI}} < 12$ MeV energy gates. The spectra have been normalized to the on-resonance run time of 61.15 h. The regions in red (blue) correspond to the signal (background) region(s) selected for analysis. The top panel clearly shows the 1369-keV γ ray that is attributed to the β^- -delayed γ decay of ^{24}Na . By increasing the lower bound of the energy cut, the strength of this line is reduced to a level consistent with the surrounding background.

Although Fig. 10 shows that the contribution to the 1369-keV γ ray from the β^- -delayed γ decay of ^{24}Na can be reduced, it is not immediately obvious that there is a residual signal that can be attributed to the 138-keV resonance. However, it is also possible that this state could decay directly to the ground state of ^{24}Mg via an 11831-keV transition. Figure 11 shows the on-resonance HPGe spectrum in this energy region, collected with the requirement that there be no coincidence

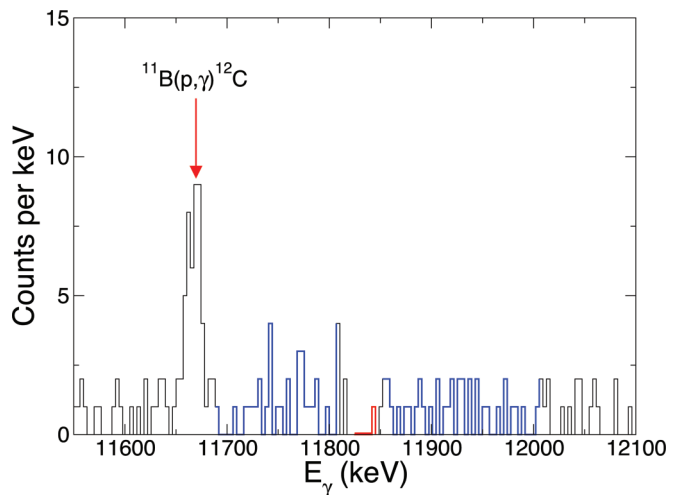


FIG. 11. (Color online) On-resonance HPGe spectrum in anticoincidence with the NaI detector, showing the energy region in the vicinity of a possible ground-state transition. The regions in red (blue) correspond to the signal (background) region(s) selected for analysis. The location of the signal region included corrections for nuclear recoil and Doppler shift.

TABLE III. Upper limit of the number of net signal counts for the 1369-keV region for several different confidence intervals of the on-resonance, off-resonance, and background data. The upper limits were calculated by integrating the posterior distribution from zero to the specified confidence level.

Coincidence gate (MeV) ^a	Spectrum ^b	Confidence level (%)			
		68	90	95	99.7
3–12	On	56.8	73.2	80.5	100.8
	Off	49.6	65.1	72.0	91.2
	Back	51.3	67.1	74.1	93.7
5–12	On	31.2	42.7	47.9	62.3
	Off	17.3	26.9	31.2	41.2
	Back	16.4	25.8	30.0	39.3

^aFor example, 3–12 MeV refers to $3 \text{ MeV} < E^{\text{Ge}} + E^{\text{NaI}} < 12 \text{ MeV}$.

^bPulse-height spectrum used for analysis, e.g., “On” refers to on-resonance.

with the NaI detector. The expected location of this transition (corrected for the effects of nuclear recoil and Doppler shift) is indicated and clearly no evidence for it is apparent.

B. Results

Since there was no clear evidence for a well-resolved peak in the on-resonance coincidence spectrum, a method employing Bayesian statistics [35] was used to extract the upper limit on the number of signal counts in the region of interest. As part of this procedure, a prior probability density function (PDF), $\pi(s)$, is assumed for the unknown signal and reflects previous knowledge of the signal parameter. Here we adopt a Cousins prior [36] for this PDF,

$$\pi(s) \propto \frac{1}{(s+b)^m}, \quad s \geq 0, \quad 0 \leq m \leq 1, \quad (3)$$

where s and b are the number of signal and background counts, respectively, and $m = 1/2$ was chosen, which provides reasonable mean coverage for the confidence interval and upper limit for a Poisson observable [35]. The advantage to this approach is the inclusion of a statistically meaningful uncertainty in the number of signal counts and background counts. The background distribution was represented by a Gaussian PDF and the same background and signal ranges were selected for specified confidence intervals in each of the data sets as shown in Figs. 8, 9, and 10.

The net signal count intensities were calculated by integrating the posterior distribution from zero counts to the specified confidence level and are listed in Table III. The corresponding posterior distributions are shown in Fig. 12, in which the black, red, and blue lines correspond to the on-resonance, off-resonance, and background data, respectively.

For the coincidence energy cuts with a lower bound of less than 5 MeV, the posterior distributions of all data subsets show evidence for a signal, which arises at least in part from the β^- decay of ^{24}Na . As the lower bound of the energy cut is increased to 5 MeV, the signal counts of the off-resonance

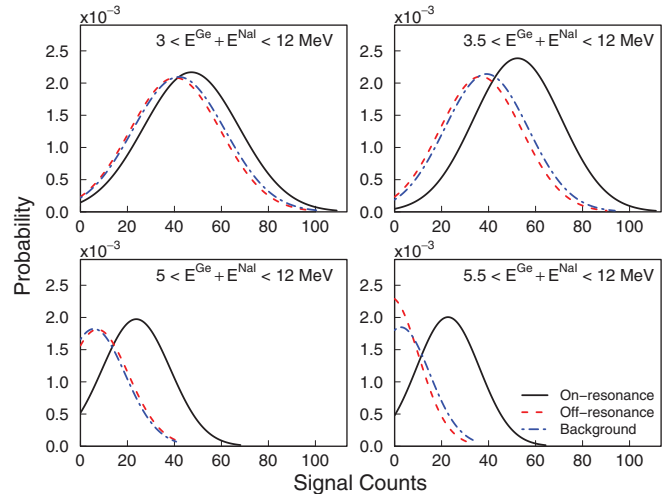


FIG. 12. (Color online) Posterior distributions for the net signal intensity in the region of interest ($E_\gamma = 1369$ keV). Each plot was obtained for a particular coincidence energy gate of the on-resonance, off-resonance, and background data subsets in black, red, and blue, respectively. The same background and signal regions were chosen to compute all posterior distributions (see Figs. 8, 9, and 10). With a $3 \text{ MeV} < E^{\text{Ge}} + E^{\text{NaI}} < 12 \text{ MeV}$ gate, all data sets show a peak, arising from ^{24}Na . As the lower boundary of the coincidence gate is increased, the off-resonance and background posterior distributions become more consistent with zero, but the on-resonance distribution remains removed from zero. With a $5 \text{ MeV} < E^{\text{Ge}} + E^{\text{NaI}} < 12 \text{ MeV}$ gate, the contribution from ^{24}Na is removed because of Q -value considerations.

and background data become more consistent with zero, indicating that this source of background has been reduced to an insignificant level. However, the mean number of counts for the on-resonance data are still greater than zero, implying a residual signal in the on-resonance data. In order to determine how far the peak of the posterior distribution was removed from zero, it was integrated in a top-down manner, that is, from the most probable value to the left and right, keeping the area on both sides of the most probable point the same (as shown in Fig. 13). At 90% coverage, the $5 \text{ MeV} < E^{\text{Ge}} + E^{\text{NaI}} < 12 \text{ MeV}$ on-resonance signal distribution is removed from zero. However, at the $2 - \sigma$ level (95%) the distribution is consistent with zero. Thus, while there is a preference for a signal at the 90% CL, we treat this result as an upper limit at the 95% CL. Assuming an upper limit for the number of signal events, the resonance strength can be expressed as [12]

$$\omega \gamma_{\text{UL}}(138 \text{ keV}) \leq \frac{2}{\lambda_r^2} \varepsilon_{\text{eff}}^{\text{cm}} \frac{1}{N_b} \left[\frac{N_{R \rightarrow 0}^V}{\eta_{R \rightarrow 0}^{\text{Ge}, P}} + \frac{N_{1 \rightarrow 0}^C}{\eta_{1 \rightarrow 0}^{\text{Ge}, P}} \frac{1}{f_\gamma} \right], \quad (4)$$

where λ_r is the deBroglie wavelength, $\varepsilon_{\text{eff}}^{\text{cm}}$ is the effective stopping power, and N_b is the number of beam particles. The first term in the brackets corresponds to the contribution from a ground-state transition, $R \rightarrow 0$, with $N_{R \rightarrow 0}$ observed events and a peak detection efficiency, $\eta_{R \rightarrow 0}^{\text{Ge}, P}$. The second term

corresponds to the contributions from γ -ray cascades through the first excited to ground-state transition, $1 \rightarrow 0$, with $N_{1 \rightarrow 0}^C$ coincidence counts and a peak detection efficiency $\eta_{1 \rightarrow 0}^{\text{Ge},P}$. The quantity f_γ , is the coincidence efficiency of the HPGe-NaI(Tl) detection system for measuring a $E_\gamma = 1369$ keV γ ray from the $1 \rightarrow 0$ transition in ^{24}Mg . The number of signal counts in the 11831-keV region for the ground-state transition was obtained using the Bayesian technique on the HPGe pulse-height spectrum for the regions selected in Fig. 11. The number of signal events at 95% confidence level was $N_{R \rightarrow 0} \leq 3$. The number of signal events in the $5 \text{ MeV} < E^{\text{Ge}} + E^{\text{NaI}} < 12 \text{ MeV}$ coincidence spectrum was $N_{1 \rightarrow 0}^C \leq 47.9$ at 95% confidence level (see Table III). The mean coincidence efficiency for detecting the 1369-keV γ ray, based on the known decays of 36 states above $E_x = 9.0$ MeV excitation energy (all with ground-state branches less than 47% of the total decay strength and with greater than 27% of the total branching known) is $f_\gamma = 0.379(66)$ for an energy gate of $5 < E^{\text{Ge}} + E^{\text{NaI}} < 12 \text{ MeV}$. Thus, the upper limit to the resonance strength is $\omega\gamma_{\text{UL}}(138 \text{ keV}) \leq 5.17 \times 10^{-9} \text{ eV}$, a reduction of the previous upper limit by a factor of 29. This limit accounts for uncertainties in detection efficiencies, f_γ , $\epsilon_{\text{eff}}^{\text{cm}}$ (5% in stoichiometry and 5% in stopping power) and N_b (3%). However, if we were to interpret the PDF shown in Fig. 13 as a positive detection of the resonance, then the resulting resonance strength would be $\omega\gamma(138 \text{ keV}) = 2.15 \pm 1.29 \times 10^{-9} \text{ eV}$ (68% confidence interval).

It should be noted that by comparing $\omega\gamma_{\text{UL}}(138 \text{ keV}) \leq 5.17 \times 10^{-9} \text{ eV}$ (95% CL) with the entries in Table I, it appears that population of the 11831-keV state in ^{24}Mg via s - or p -wave proton capture is ruled out. A new reaction rate for the $^{23}\text{Na}(p,\gamma)^{24}\text{Mg}$ reaction was calculated using this result.

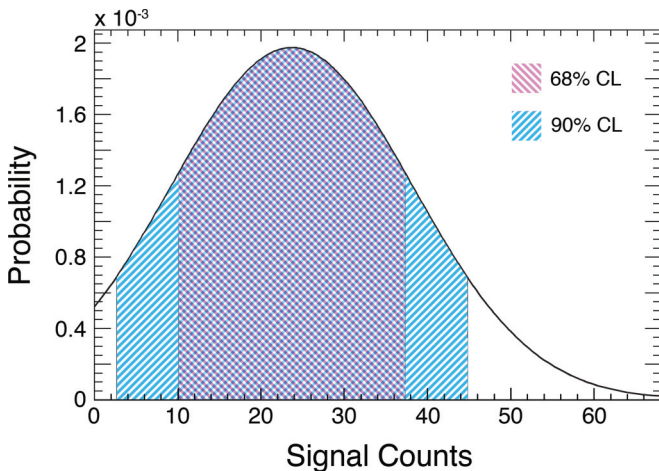


FIG. 13. (Color online) Posterior distribution for the number of signal counts in the 1369-keV region of the on-resonance coincidence spectrum with an energy gate of $5 < E^{\text{Ge}} + E^{\text{NaI}} < 12 \text{ MeV}$. This is the same distribution as shown in black of Fig. 12 (bottom left). For the purposes of illustration, the 68% and 90% confidence ranges are shown. To obtain an upper limit on the number of counts, this distribution was integrated upward from zero.

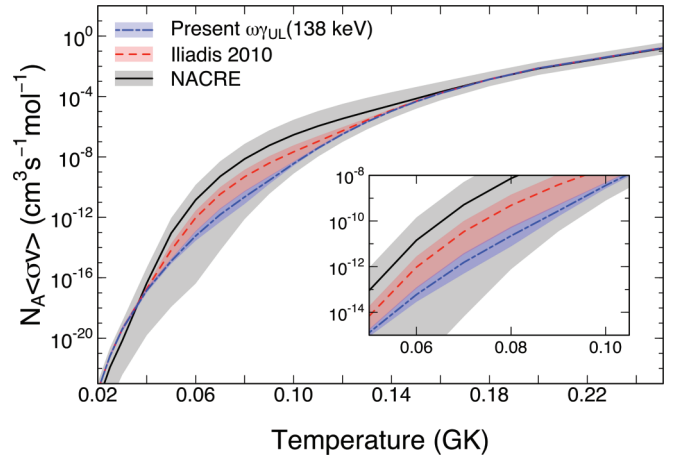


FIG. 14. (Color online) The $^{23}\text{Na}(p,\gamma)^{24}\text{Mg}$ reaction rate versus temperature. Existing compilations (NACRE [37] in black and Iliadis *et al.* [18] in red) are compared to the present total reaction rate. The blue line corresponds to the new median rate calculated using $\omega\gamma_{\text{UL}}(138 \text{ keV}) \leq 5.17 \times 10^{-9} \text{ eV}$. The inset of the plot shows an expanded view of the temperature region where the new rates have the most significant impact. The shaded regions correspond to the uncertainties associated with each rate.

IV. ASTROPHYSICAL CONSIDERATIONS

A. Thermonuclear reaction rates

The thermonuclear reaction rate is the product of cross section and relative velocity, averaged over a Maxwell-Boltzmann velocity distribution of particles in a stellar plasma. For a narrow resonance at $E_r^{\text{c.m.}}$, the rate can be expressed as

$$N_A \langle \sigma v \rangle = N_A \left(\frac{2\pi}{\mu kT} \right)^{3/2} \hbar^2 \omega\gamma e^{-E_r^{\text{c.m.}}/kT}, \quad (5)$$

where N_A is Avogadro's number, μ is the reduced mass, k is the Boltzmann constant, and $\omega\gamma$ is the resonance strength. The most recent calculation [18] of the $^{23}\text{Na}+p$ reaction rates employed a Monte Carlo approach to produce statistically meaningful uncertainties, using the code RATESMC [19]. We have adopted the same computational method for the new calculations presented here. Each nuclear quantity is represented by a probability-density function (PDF), which is sampled many times over the course of the calculation. In particular, the value of $\omega\gamma_{\text{UL}} \leq 5.17 \times 10^{-9} \text{ eV}$ with $l_p = 2$ for the 138-keV resonance was used to generate a Porter-Thomas distribution for the resonance strength, and the resonance energy, $138.0 \pm 1.4 \text{ keV}$, was assigned a Gaussian PDF. The final reaction rate is closely described by a log-normal PDF where the low, median, and high rates correspond to the 0.16, 0.5, and 0.84 quantiles of the cumulative distribution, respectively. The rate limits between the 0.16 and 0.84 quantiles correspond to a 68% coverage of the cumulative distribution and represent the uncertainty in the rate.

1. $^{23}\text{Na}(p,\gamma)^{24}\text{Mg}$

The $^{23}\text{Na}(p,\gamma)^{24}\text{Mg}$ reaction rate is dominated by contributions from direct capture and low-energy resonances

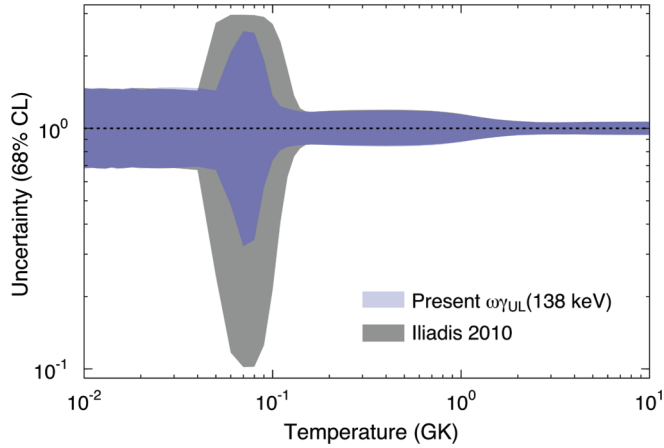


FIG. 15. (Color online) The $^{23}\text{Na}(p,\gamma)^{24}\text{Mg}$ reaction rate uncertainty versus temperature. The grey region corresponds to the previous uncertainty band [18] while the blue area is the uncertainty calculated using $\omega_{\gamma_{\text{UL}}}(138 \text{ keV}) \leq 5.17 \times 10^{-9} \text{ eV}$ for the 138-keV resonance.

[18]. The input quantities for direct capture and resonances other than the 138-keV resonance were kept as listed in Ref. [18]. The resulting rate with uncertainties is listed in Table IV of the appendix. The first column indicates the temperature in GK, the second, third, and fourth columns are the low (0.16 quantile), median (0.50 quantile), and high (0.84 quantile) rates, respectively. The fifth and sixth columns represent μ and σ for the lognormal distribution of the rate, which can be expressed in terms of these quantities by

$$N_A \langle \sigma v \rangle_{\text{low}} = e^{(\mu - \sigma)},$$

$$N_A \langle \sigma v \rangle_{\text{med}} = e^{\mu}, \quad N_A \langle \sigma v \rangle_{\text{high}} = e^{(\mu + \sigma)}. \quad (6)$$

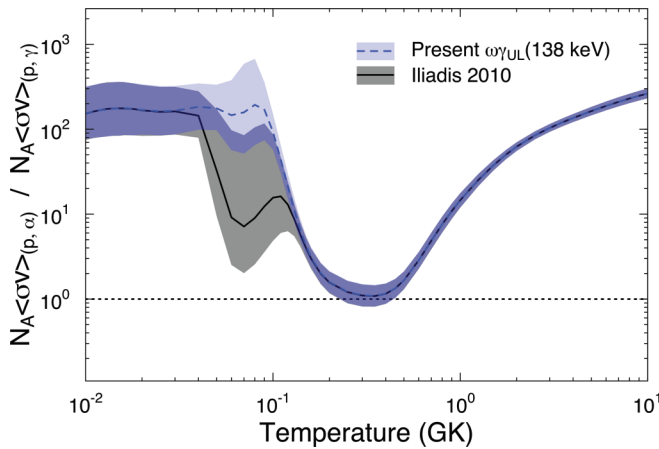


FIG. 16. (Color online) The $(p,\alpha)/(p,\gamma)$ reaction rate ratio. The solid lines correspond to the ratio of median rates. The shaded regions are $1-\sigma$ uncertainty bands that correspond to the correlated uncertainties in the low and high rates, i.e., the upper bound of the shaded region corresponds to the $(p,\alpha)_{\text{high}}/(p,\gamma)_{\text{low}}$ ratio of rates and the lower bound corresponds to the $(p,\alpha)_{\text{low}}/(p,\gamma)_{\text{high}}$ ratio. The black curve represents the previous results [18]. The dashed blue curve represents the present ratio using the present upper limit on the strength of the 138-keV resonance.

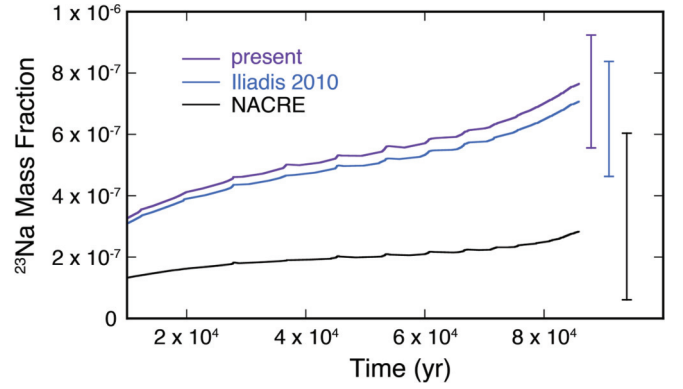


FIG. 17. (Color online) The evolution of ^{23}Na at the base of the convective envelope during AGB evolution, calculated using the temperature/density profile for the $5 M_{\odot}$, $Z \sim 10^{-3}$ model of Refs. [39,40]. Time is measured from the start of thermal pulsing. The present result is denoted by the purple line and those calculated using rates taken from Refs. [18,37] are shown in blue and black, respectively. In each case, the 16–84% uncertainty in the final abundance is denoted by the vertical error bar.

Column seven lists the Anderson-Darling test statistic, which measures the reliability of the lognormal approximation [18].

Figure 14 shows the rates from the NACRE compilation [37], Iliadis *et al.* [18], and from the present study, in the temperature region where the 138-keV resonance has the greatest impact. The NACRE rate, which has been widely used, is based on measurements made before 1999 and thus excludes the work of Hale *et al.* [15] and Rowland *et al.* [12]. The results of those measurements were included in the later compilation of Iliadis *et al.* [18] and significantly reduced the uncertainty in the rate for $T_9 \approx 0.03\text{--}0.1$. Our present measurement reduces both the value of the rate and its uncertainty in this temperature

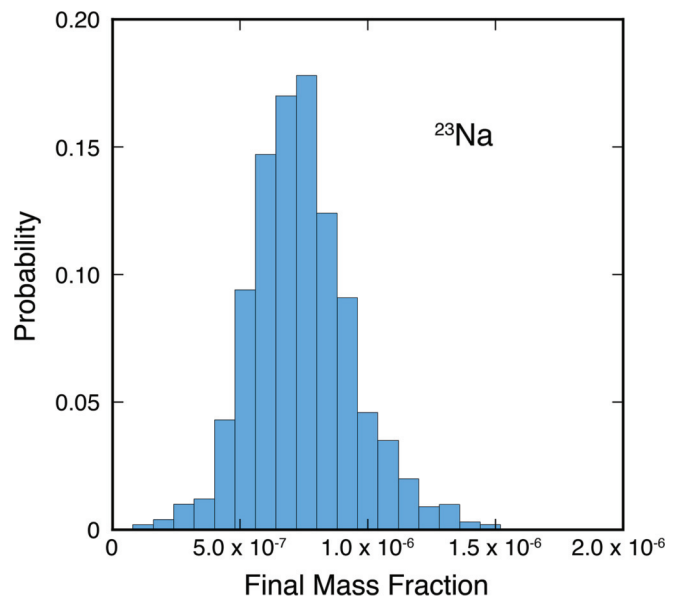


FIG. 18. (Color online) The probability density of the final ^{23}Na abundance calculated using the present results.

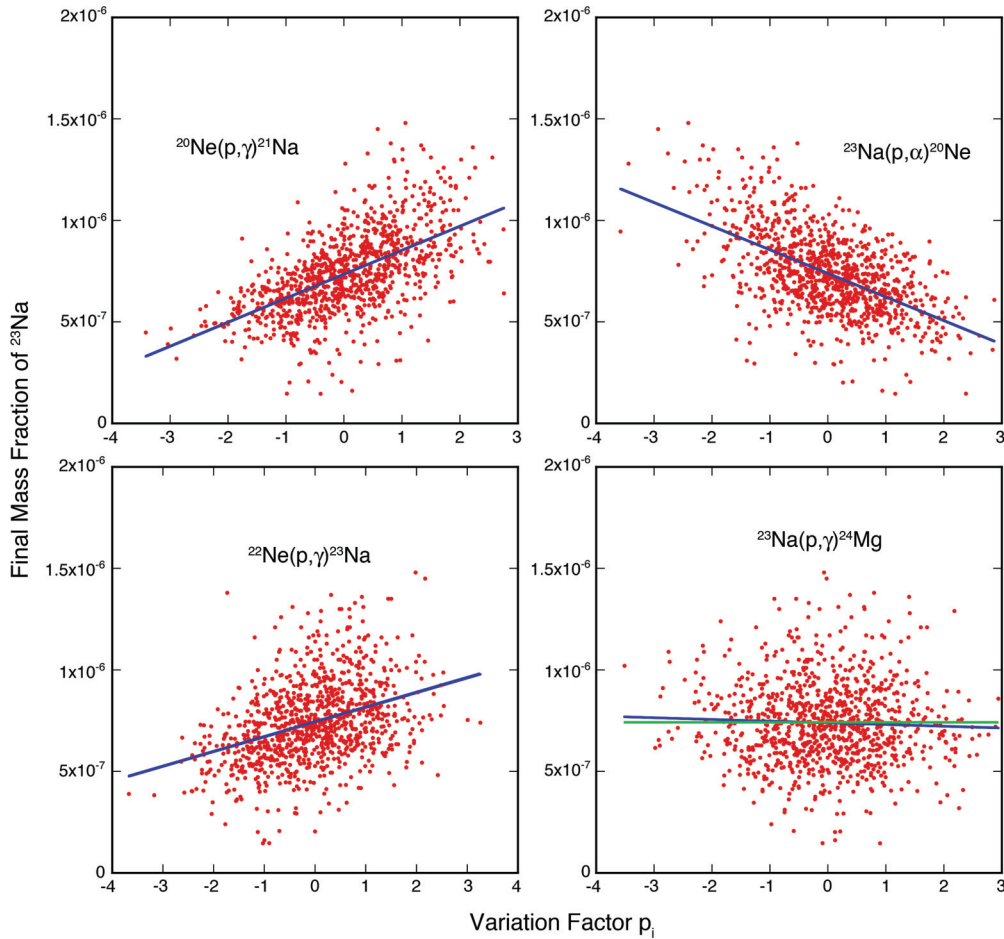


FIG. 19. (Color online) Correlations between the final abundance of ^{23}Na and the rate-variation factor p_i for each of the 1000 samples of the reaction network. The blue lines are linear fits to the correlations. In the case of the $^{23}\text{Na}(p,\gamma)^{24}\text{Mg}$ reaction, the green (horizontal) line would be consistent with no correlation.

range. For example, our median rate is a factor 5.6–22.9 lower than that of Ref. [18] for $T_9 = 0.05\text{--}0.10$.

The 68% uncertainty regions for the rate is shown in Fig. 15. The gray area represents the uncertainty in the rate as calculated from previous results [18], whereas the blue area is the uncertainty calculated with $\omega\gamma_{\text{UL}}(138\text{ keV}) \leq 5.17 \times 10^{-9}\text{ eV}$ for the 138-keV resonance. The uncertainty in the rate is reduced, from a factor of 28 at $T_9 = 0.07$ to a factor of 7.8.

2. $^{23}\text{Na}(p,\alpha)^{20}\text{Ne}$

We also calculate a revised $^{23}\text{Na}(p,\alpha)^{20}\text{Ne}$ rate. However, since $\Gamma_\gamma/\Gamma = 0.95(4)$ for the $E_x = 11831\text{ keV}$ state [38], proton capture via the 138-keV resonance proceeds primarily through the (p,γ) channel; evidence for α decay is significant only at the $1 - \sigma$ level. Thus, the contribution of the 138-keV resonance is calculated based on the upper limit for the resonance strength in the (p,γ) channel,

$$\omega\gamma_{p\alpha} = \omega\Gamma_{p\gamma} \times \frac{\Gamma_\alpha}{\Gamma}, \quad (7)$$

with $\omega\Gamma_{p\gamma} \leq 5.17 \times 10^{-9}\text{ eV}$ and $\Gamma_\alpha/\Gamma = 0.05 \pm 0.04$. Treating the latter quantity as an upper limit, i.e., $\Gamma_\alpha/\Gamma \leq$

0.13 (95% CL) yields $\omega\gamma_{p\alpha} \leq 0.88 \times 10^{-9}\text{ eV}$, which implies a negligible contribution to the reaction rate. Consequently, our recommended rate for the $^{23}\text{Na}(p,\alpha)^{20}\text{Ne}$ reaction does not include a contribution from the 138-keV resonance. The resulting rate (Table V) is in excellent agreement with that tabulated in Ref. [18].

3. $(p,\alpha)/(p,\gamma)$ reaction rate ratio

As ^{23}Na is destroyed by $^{23}\text{Na}+p$, material can leak into the MgAl region, by emission of γ rays, or recycle back to the NeNa cycle via the $^{20}\text{Ne}+\alpha$ channel. Figure 16 shows the ratio of the $(p,\alpha)/(p,\gamma)$ median rates. The shaded regions correspond to $1-\sigma$ uncertainty bands representing the uncertainties of the ratio, i.e., the upper end of the shaded region corresponds to the $(p,\alpha)_{\text{high}}/(p,\gamma)_{\text{low}}$ ratio of rates and the lower corresponds to the $(p,\alpha)_{\text{low}}/(p,\gamma)_{\text{high}}$ ratio. The ratio using the previous $^{23}\text{Na}(p,\gamma)^{24}\text{Mg}$ and $^{23}\text{Na}(p,\alpha)^{20}\text{Ne}$ rates from Ref. [18] are plotted in black. The blue line corresponds to the present upper limit for the 138-keV resonance strength and it is clear that the uncertainty of the ratio has been reduced dramatically. The largest changes in the ratio are $T_9 = 0.05\text{--}0.11$ and over that range the median ratio is larger than the previous upper ratio bound. At $T_9 = 0.07$,

the present ratio is a factor of 22 greater and, thus, leakage into the MgAl chain is ~ 22 times slower than previously thought.

B. Nucleosynthesis calculations

In order to explore the impact of these new results, we have performed one-zone postprocessing calculations using a $5 M_{\odot}$, $Z \sim 10^{-3}$ AGB model from Ventura and D'Antona [39,40]. The calculations used the temperature-density profile at the base of the convective envelope and did not include any mixing between thermal pulses. Consequently, they are not meant to represent observable surface abundances but merely to show the effect of the present results at the base of the convective envelope. The average temperature in this profile was $T_9 = 0.078$, with a maximum of $T_9 = 0.10$, temperatures where the 138-keV resonance is situated to have its maximum impact. The time evolution of ^{23}Na is shown in Fig. 17, which follows from the beginning of the thermal-pulsing stage (at $t = 0$) through to the end of last pulse. Reaction rates were taken from the STARLIB compilation [41] with the exception of the rates for the $^{23}\text{Na}(p,\gamma)^{24}\text{Mg}$ and $^{23}\text{Na}(p,\alpha)^{20}\text{Ne}$ reactions. For these we have used our present results and those from Refs. [18,37]. The uncertainties in the final abundances, assuming a 68% coverage probability, were calculated using a Monte Carlo procedure [42] in which the rates for all 1657 reactions in the network were sampled simultaneously and independently. This was done by introducing a variation factor, p_i , for each reaction, which is a randomly sampled multiplier of the log-normal standard deviation for each reaction [41,42]. The results shown here were obtained from 1000 samples of each of the three reaction networks. Figure 17 shows that the current reduction in the $^{23}\text{Na}(p,\gamma)^{24}\text{Mg}$ rate leads to increased ^{23}Na production, as would be expected, but by a statistically insignificant amount (13%) over what was expected from the rates found in Ref. [18], despite the significant reduction in the rate of the $^{23}\text{Na}(p,\gamma)^{24}\text{Mg}$ reaction. On the other hand, the final ^{23}Na abundance is about 2.5 times greater than that calculated using the NACRE rates [37]. The probability density of the final ^{23}Na abundance calculated using the present results is shown in Fig. 18. It should be noted that this distribution is determined by the uncertainties in all rates, not just those for the $^{23}\text{Na}(p,\gamma)^{24}\text{Mg}$ and $^{23}\text{Na}(p,\alpha)^{20}\text{Ne}$ reactions and thus can be used to determine a median value and uncertainty at any desired confidence level.

As noted above, the uncertainties shown in Fig. 17 arise from all of the reaction-rate uncertainties in the reaction network and clearly the reduction in the uncertainty of the $^{23}\text{Na}(p,\gamma)^{24}\text{Mg}$ reaction over the rate tabulated in Ref. [18] does not produce a commensurate reduction in the uncertainty of the final abundance. Clearly, other reactions are important. Figure 19 shows the correlation between the final ^{23}Na abundance and the rate of the key reactions that determine the abundance, expressed in terms of the variation factor p_i for each reaction. In this case, there were 1000 simultaneous samples of each reaction in the network. As is clear in Fig. 19, the reactions that have the largest impact on the ^{23}Na abundance are (in order of the slope of the correlation) $^{20}\text{Ne}(p,\gamma)^{21}\text{Na}$, $^{23}\text{Na}(p,\alpha)^{20}\text{Ne}$, and $^{22}\text{Ne}(p,\gamma)^{23}\text{Na}$. In contrast, the $^{23}\text{Na}(p,\gamma)^{24}\text{Mg}$ reaction has negligible impact on the abundance of ^{23}Na . This can be understood by reference to Fig. 16, which shows that the $^{23}\text{Na}(p,\alpha)^{20}\text{Ne}$ reaction now dominates the $^{23}\text{Na}(p,\gamma)^{24}\text{Mg}$ reaction for the temperatures considered here.

V. CONCLUSION

We have set an upper limit on the strength of the 138-keV resonance in the $^{23}\text{Na}(p,\gamma)^{24}\text{Mg}$ reaction of $\omega\gamma_{\text{UL}}(138 \text{ keV}) \leq 5.17 \times 10^{-9}$ eV (95% CL). This significantly reduces the rate of the $^{23}\text{Na}(p,\gamma)^{24}\text{Mg}$ reaction for temperatures characteristic of AGB stars, to the point where this reaction has a negligible influence on the abundance of ^{23}Na . In addition, the NeNa cycle is essentially closed for temperatures below about $T_9 = 0.1$ and thus has no influence on nucleosynthesis in the MgAl region. Further work on the reactions that impact the O-Na anomaly in globular clusters should focus on the $^{20}\text{Ne}(p,\gamma)^{21}\text{Na}$, $^{23}\text{Na}(p,\alpha)^{20}\text{Ne}$, and $^{22}\text{Ne}(p,\gamma)^{23}\text{Na}$ reactions.

ACKNOWLEDGMENTS

This work was supported in part by the U.S. Department of Energy under Contract No. DE-FG02-97ER41041 and by the U.S. Department of Energy National Nuclear Security Administration under Contract No. DE-FC52-08NA28752. We also thank R. G. Izzard and P. Ventura for their helpful input.

APPENDIX: REACTION RATES FOR $^{23}\text{Na}(p,\gamma)^{24}\text{Mg}$ AND $^{23}\text{Na}(p,\alpha)^{20}\text{Ne}$

TABLE IV. Reaction rates of $^{23}\text{Na}(p,\gamma)^{24}\text{Mg}$, calculated with the code RATESMC, using a Monte Carlo method. The $E_r^{c.m.} = 138$ keV resonance strength of $^{23}\text{Na}(p,\gamma)^{24}\text{Mg}$ is represented by an upper limit, $\omega\gamma_{\text{UL}}(138 \text{ keV}) \leq 5.17 \times 10^{-9}$ eV.

T (GK)	Low rate	Median rate	High rate	Lognormal μ	Lognormal σ	A-D
0.010	8.29×10^{-33}	1.22×10^{-32}	1.77×10^{-32}	$-7.349 \times 10^{+01}$	3.80×10^{-01}	3.25×10^{-01}
0.011	1.59×10^{-31}	2.32×10^{-31}	3.39×10^{-31}	$-7.054 \times 10^{+01}$	3.81×10^{-01}	1.69×10^{-01}
0.012	2.16×10^{-30}	3.19×10^{-30}	4.66×10^{-30}	$-6.792 \times 10^{+01}$	3.82×10^{-01}	4.85×10^{-01}
0.013	2.25×10^{-29}	3.27×10^{-29}	4.80×10^{-29}	$-6.558 \times 10^{+01}$	3.81×10^{-01}	4.32×10^{-01}
0.014	1.83×10^{-28}	2.70×10^{-28}	3.91×10^{-28}	$-6.348 \times 10^{+01}$	3.83×10^{-01}	5.73×10^{-01}
0.015	1.25×10^{-27}	1.81×10^{-27}	2.65×10^{-27}	$-6.157 \times 10^{+01}$	3.84×10^{-01}	2.72×10^{-01}
0.016	7.09×10^{-27}	1.05×10^{-26}	1.54×10^{-26}	$-5.982 \times 10^{+01}$	3.86×10^{-01}	5.96×10^{-01}

TABLE IV. (*Continued.*)

T (GK)	Low rate	Median rate	High rate	Lognormal μ	Lognormal σ	A-D
0.018	1.56×10^{-25}	2.29×10^{-25}	3.37×10^{-25}	$-5.673 \times 10^{+01}$	3.85×10^{-01}	4.08×10^{-01}
0.020	2.23×10^{-24}	3.28×10^{-24}	4.87×10^{-24}	$-5.407 \times 10^{+01}$	3.88×10^{-01}	6.61×10^{-01}
0.025	4.65×10^{-22}	6.83×10^{-22}	1.00×10^{-21}	$-4.873 \times 10^{+01}$	3.81×10^{-01}	$1.02 \times 10^{+00}$
0.030	2.75×10^{-20}	3.99×10^{-20}	5.79×10^{-20}	$-4.467 \times 10^{+01}$	3.79×10^{-01}	2.63×10^{-01}
0.040	1.02×10^{-17}	1.50×10^{-17}	2.17×10^{-17}	$-3.874 \times 10^{+01}$	3.77×10^{-01}	2.51×10^{-01}
0.050	8.61×10^{-16}	1.28×10^{-15}	1.85×10^{-15}	$-3.431 \times 10^{+01}$	3.78×10^{-01}	$4.79 \times 10^{+00}$
0.060	2.88×10^{-14}	6.03×10^{-14}	1.26×10^{-13}	$-3.046 \times 10^{+01}$	6.58×10^{-01}	$4.92 \times 10^{+01}$
0.070	5.03×10^{-13}	1.56×10^{-12}	3.95×10^{-12}	$-2.728 \times 10^{+01}$	8.94×10^{-01}	$9.82 \times 10^{+01}$
0.080	7.81×10^{-12}	2.26×10^{-11}	5.70×10^{-11}	$-2.457 \times 10^{+01}$	8.49×10^{-01}	$1.10 \times 10^{+02}$
0.090	1.58×10^{-10}	2.78×10^{-10}	5.43×10^{-10}	$-2.198 \times 10^{+01}$	5.43×10^{-01}	$6.62 \times 10^{+01}$
0.100	2.63×10^{-09}	3.58×10^{-09}	4.90×10^{-09}	$-1.945 \times 10^{+01}$	2.99×10^{-01}	$6.71 \times 10^{+00}$
0.110	3.12×10^{-08}	3.83×10^{-08}	4.77×10^{-08}	$-1.707 \times 10^{+01}$	2.16×10^{-01}	$1.39 \times 10^{+00}$
0.120	2.68×10^{-07}	3.21×10^{-07}	3.89×10^{-07}	$-1.495 \times 10^{+01}$	1.88×10^{-01}	$3.37 \times 10^{+00}$
0.130	1.77×10^{-06}	2.08×10^{-06}	2.48×10^{-06}	$-1.308 \times 10^{+01}$	1.72×10^{-01}	$1.86 \times 10^{+00}$
0.140	9.16×10^{-06}	1.07×10^{-05}	1.26×10^{-05}	$-1.144 \times 10^{+01}$	1.63×10^{-01}	7.57×10^{-01}
0.150	3.87×10^{-05}	4.52×10^{-05}	5.30×10^{-05}	$-1.000 \times 10^{+01}$	1.59×10^{-01}	3.65×10^{-01}
0.160	1.38×10^{-04}	1.61×10^{-04}	1.88×10^{-04}	$-8.736 \times 10^{+00}$	1.58×10^{-01}	2.22×10^{-01}
0.180	1.15×10^{-03}	1.34×10^{-03}	1.58×10^{-03}	$-6.612 \times 10^{+00}$	1.60×10^{-01}	1.38×10^{-01}
0.200	6.27×10^{-03}	7.38×10^{-03}	8.67×10^{-03}	$-4.910 \times 10^{+00}$	1.63×10^{-01}	1.28×10^{-01}
0.250	1.31×10^{-01}	1.55×10^{-01}	1.83×10^{-01}	$-1.866 \times 10^{+00}$	1.68×10^{-01}	1.52×10^{-01}
0.300	9.58×10^{-01}	$1.14 \times 10^{+00}$	$1.35 \times 10^{+00}$	1.280×10^{-01}	1.71×10^{-01}	1.98×10^{-01}
0.350	$3.86 \times 10^{+00}$	$4.59 \times 10^{+00}$	$5.44 \times 10^{+00}$	$1.522 \times 10^{+00}$	1.72×10^{-01}	2.17×10^{-01}
0.400	$1.07 \times 10^{+01}$	$1.28 \times 10^{+01}$	$1.51 \times 10^{+01}$	$2.545 \times 10^{+00}$	1.73×10^{-01}	2.27×10^{-01}
0.450	$2.34 \times 10^{+01}$	$2.78 \times 10^{+01}$	$3.29 \times 10^{+01}$	$3.323 \times 10^{+00}$	1.73×10^{-01}	2.29×10^{-01}
0.500	$4.30 \times 10^{+01}$	$5.11 \times 10^{+01}$	$6.05 \times 10^{+01}$	$3.933 \times 10^{+00}$	1.72×10^{-01}	2.22×10^{-01}
0.600	$1.05 \times 10^{+02}$	$1.25 \times 10^{+02}$	$1.47 \times 10^{+02}$	$4.825 \times 10^{+00}$	1.68×10^{-01}	1.98×10^{-01}
0.700	$1.98 \times 10^{+02}$	$2.33 \times 10^{+02}$	$2.73 \times 10^{+02}$	$5.450 \times 10^{+00}$	1.62×10^{-01}	1.93×10^{-01}
0.800	$3.20 \times 10^{+02}$	$3.72 \times 10^{+02}$	$4.33 \times 10^{+02}$	$5.919 \times 10^{+00}$	1.53×10^{-01}	2.53×10^{-01}
0.900	$4.68 \times 10^{+02}$	$5.40 \times 10^{+02}$	$6.22 \times 10^{+02}$	$6.291 \times 10^{+00}$	1.43×10^{-01}	4.13×10^{-01}
1.000	$6.45 \times 10^{+02}$	$7.35 \times 10^{+02}$	$8.39 \times 10^{+02}$	$6.601 \times 10^{+00}$	1.32×10^{-01}	6.63×10^{-01}
1.250	$1.21 \times 10^{+03}$	$1.35 \times 10^{+03}$	$1.50 \times 10^{+03}$	$7.208 \times 10^{+00}$	1.07×10^{-01}	$1.22 \times 10^{+00}$
1.500	$1.97 \times 10^{+03}$	$2.15 \times 10^{+03}$	$2.35 \times 10^{+03}$	$7.675 \times 10^{+00}$	8.73×10^{-02}	9.87×10^{-01}
1.750	$2.93 \times 10^{+03}$	$3.15 \times 10^{+03}$	$3.40 \times 10^{+03}$	$8.056 \times 10^{+00}$	7.47×10^{-02}	7.65×10^{-01}
2.000	$4.06 \times 10^{+03}$	$4.34 \times 10^{+03}$	$4.64 \times 10^{+03}$	$8.375 \times 10^{+00}$	6.71×10^{-02}	5.05×10^{-01}
2.500	$6.73 \times 10^{+03}$	$7.14 \times 10^{+03}$	$7.58 \times 10^{+03}$	$8.874 \times 10^{+00}$	6.01×10^{-02}	2.39×10^{-01}
3.000	$9.68 \times 10^{+03}$	$1.02 \times 10^{+04}$	$1.09 \times 10^{+04}$	$9.236 \times 10^{+00}$	5.83×10^{-02}	4.55×10^{-01}
3.500	$1.26 \times 10^{+04}$	$1.34 \times 10^{+04}$	$1.42 \times 10^{+04}$	$9.501 \times 10^{+00}$	5.83×10^{-02}	3.91×10^{-01}
4.000	$1.53 \times 10^{+04}$	$1.63 \times 10^{+04}$	$1.72 \times 10^{+04}$	$9.696 \times 10^{+00}$	5.88×10^{-02}	2.70×10^{-01}
5.000	$1.97 \times 10^{+04}$	$2.10 \times 10^{+04}$	$2.22 \times 10^{+04}$	$9.950 \times 10^{+00}$	6.02×10^{-02}	2.16×10^{-01}
6.000	$2.27 \times 10^{+04}$	$2.41 \times 10^{+04}$	$2.56 \times 10^{+04}$	$1.009 \times 10^{+01}$	6.12×10^{-02}	2.19×10^{-01}
7.000	$2.45 \times 10^{+04}$	$2.60 \times 10^{+04}$	$2.77 \times 10^{+04}$	$1.017 \times 10^{+01}$	6.19×10^{-02}	2.22×10^{-01}
8.000	$2.54 \times 10^{+04}$	$2.70 \times 10^{+04}$	$2.87 \times 10^{+04}$	$1.020 \times 10^{+01}$	6.24×10^{-02}	2.46×10^{-01}
9.000	$2.57 \times 10^{+04}$	$2.73 \times 10^{+04}$	$2.91 \times 10^{+04}$	$1.022 \times 10^{+01}$	6.27×10^{-02}	2.62×10^{-01}
10.000	$2.55 \times 10^{+04}$	$2.72 \times 10^{+04}$	$2.89 \times 10^{+04}$	$1.021 \times 10^{+01}$	6.29×10^{-02}	2.77×10^{-01}

TABLE V. Reaction rates of $^{23}\text{Na}(p,\alpha)^{20}\text{Ne}$ calculated with RATESMC, using a Monte Carlo method. The $E_r^{c.m.} = 138$ keV resonance of $^{23}\text{Na}(p,\alpha)^{20}\text{Ne}$ has a negligible influence on the rate and is not included.

T (GK)	Low rate	Median rate	High rate	Lognormal μ	Lognormal σ	A-D
0.010	1.35×10^{-30}	1.87×10^{-30}	2.65×10^{-30}	$-6.844 \times 10^{+01}$	3.36×10^{-01}	$4.50 \times 10^{+00}$
0.011	2.68×10^{-29}	3.74×10^{-29}	5.27×10^{-29}	$-6.545 \times 10^{+01}$	3.38×10^{-01}	$1.48 \times 10^{+00}$
0.012	3.75×10^{-28}	5.29×10^{-28}	7.44×10^{-28}	$-6.281 \times 10^{+01}$	3.41×10^{-01}	9.09×10^{-01}
0.013	3.95×10^{-27}	5.63×10^{-27}	7.91×10^{-27}	$-6.044 \times 10^{+01}$	3.43×10^{-01}	$1.65 \times 10^{+00}$
0.014	3.29×10^{-26}	4.70×10^{-26}	6.59×10^{-26}	$-5.832 \times 10^{+01}$	3.43×10^{-01}	$2.39 \times 10^{+00}$
0.015	2.25×10^{-25}	3.21×10^{-25}	4.48×10^{-25}	$-5.640 \times 10^{+01}$	3.41×10^{-01}	$2.55 \times 10^{+00}$
0.016	1.30×10^{-24}	1.84×10^{-24}	2.56×10^{-24}	$-5.466 \times 10^{+01}$	3.36×10^{-01}	$2.13 \times 10^{+00}$
0.018	2.86×10^{-23}	3.99×10^{-23}	5.48×10^{-23}	$-5.158 \times 10^{+01}$	3.23×10^{-01}	9.77×10^{-01}
0.020	4.10×10^{-22}	5.55×10^{-22}	7.60×10^{-22}	$-4.894 \times 10^{+01}$	3.10×10^{-01}	$1.67 \times 10^{+00}$
0.025	8.48×10^{-20}	1.10×10^{-19}	1.49×10^{-19}	$-4.363 \times 10^{+01}$	2.89×10^{-01}	$9.90 \times 10^{+00}$
0.030	5.07×10^{-18}	6.50×10^{-18}	8.73×10^{-18}	$-3.956 \times 10^{+01}$	2.77×10^{-01}	$1.27 \times 10^{+01}$
0.040	2.15×10^{-15}	2.72×10^{-15}	3.56×10^{-15}	$-3.352 \times 10^{+01}$	2.57×10^{-01}	$7.48 \times 10^{+00}$
0.050	1.79×10^{-13}	2.25×10^{-13}	2.87×10^{-13}	$-2.911 \times 10^{+01}$	2.40×10^{-01}	$2.25 \times 10^{+00}$
0.060	7.01×10^{-12}	8.69×10^{-12}	1.07×10^{-11}	$-2.547 \times 10^{+01}$	2.15×10^{-01}	9.79×10^{-01}
0.070	1.99×10^{-10}	2.41×10^{-10}	2.90×10^{-10}	$-2.215 \times 10^{+01}$	1.89×10^{-01}	6.87×10^{-01}
0.080	3.63×10^{-09}	4.33×10^{-09}	5.19×10^{-09}	$-1.926 \times 10^{+01}$	1.80×10^{-01}	5.11×10^{-01}
0.090	3.97×10^{-08}	4.70×10^{-08}	5.64×10^{-08}	$-1.687 \times 10^{+01}$	1.77×10^{-01}	6.16×10^{-01}
0.100	2.82×10^{-07}	3.34×10^{-07}	3.99×10^{-07}	$-1.491 \times 10^{+01}$	1.75×10^{-01}	7.20×10^{-01}
0.110	1.45×10^{-06}	1.71×10^{-06}	2.03×10^{-06}	$-1.328 \times 10^{+01}$	1.71×10^{-01}	8.35×10^{-01}
0.120	5.88×10^{-06}	6.87×10^{-06}	8.10×10^{-06}	$-1.188 \times 10^{+01}$	1.63×10^{-01}	$1.10 \times 10^{+00}$
0.130	2.02×10^{-05}	2.33×10^{-05}	2.71×10^{-05}	$-1.066 \times 10^{+01}$	1.51×10^{-01}	$1.28 \times 10^{+00}$
0.140	6.14×10^{-05}	7.01×10^{-05}	8.04×10^{-05}	$-9.563 \times 10^{+00}$	1.38×10^{-01}	$1.13 \times 10^{+00}$
0.150	1.71×10^{-04}	1.93×10^{-04}	2.19×10^{-04}	$-8.549 \times 10^{+00}$	1.27×10^{-01}	7.20×10^{-01}
0.160	4.41×10^{-04}	4.97×10^{-04}	5.62×10^{-04}	$-7.605 \times 10^{+00}$	1.22×10^{-01}	3.12×10^{-01}
0.180	2.40×10^{-03}	2.72×10^{-03}	3.09×10^{-03}	$-5.904 \times 10^{+00}$	1.26×10^{-01}	9.78×10^{-01}
0.200	1.03×10^{-02}	1.17×10^{-02}	1.35×10^{-02}	$-4.441 \times 10^{+00}$	1.34×10^{-01}	$1.89 \times 10^{+00}$
0.250	1.65×10^{-01}	1.89×10^{-01}	2.17×10^{-01}	$-1.664 \times 10^{+00}$	1.39×10^{-01}	$2.47 \times 10^{+00}$
0.300	$1.11 \times 10^{+00}$	$1.26 \times 10^{+00}$	$1.44 \times 10^{+00}$	2.358×10^{-01}	1.32×10^{-01}	$2.91 \times 10^{+00}$
0.350	$4.46 \times 10^{+00}$	$5.02 \times 10^{+00}$	$5.68 \times 10^{+00}$	$1.616 \times 10^{+00}$	1.21×10^{-01}	$3.69 \times 10^{+00}$
0.400	$1.34 \times 10^{+01}$	$1.48 \times 10^{+01}$	$1.65 \times 10^{+01}$	$2.700 \times 10^{+00}$	1.06×10^{-01}	$4.88 \times 10^{+00}$
0.450	$3.42 \times 10^{+01}$	$3.73 \times 10^{+01}$	$4.08 \times 10^{+01}$	$3.622 \times 10^{+00}$	8.85×10^{-02}	$5.64 \times 10^{+00}$
0.500	$7.94 \times 10^{+01}$	$8.53 \times 10^{+01}$	$9.18 \times 10^{+01}$	$4.448 \times 10^{+00}$	7.34×10^{-02}	$4.05 \times 10^{+00}$
0.600	$3.37 \times 10^{+02}$	$3.57 \times 10^{+02}$	$3.81 \times 10^{+02}$	$5.880 \times 10^{+00}$	6.23×10^{-02}	$1.06 \times 10^{+00}$
0.700	$1.06 \times 10^{+03}$	$1.13 \times 10^{+03}$	$1.21 \times 10^{+03}$	$7.031 \times 10^{+00}$	6.42×10^{-02}	6.41×10^{-01}
0.800	$2.64 \times 10^{+03}$	$2.82 \times 10^{+03}$	$3.01 \times 10^{+03}$	$7.944 \times 10^{+00}$	6.62×10^{-02}	5.49×10^{-01}
0.900	$5.50 \times 10^{+03}$	$5.87 \times 10^{+03}$	$6.27 \times 10^{+03}$	$8.678 \times 10^{+00}$	6.63×10^{-02}	5.59×10^{-01}
1.000	$1.01 \times 10^{+04}$	$1.08 \times 10^{+04}$	$1.15 \times 10^{+04}$	$9.284 \times 10^{+00}$	6.51×10^{-02}	5.77×10^{-01}
1.250	$3.23 \times 10^{+04}$	$3.43 \times 10^{+04}$	$3.64 \times 10^{+04}$	$1.044 \times 10^{+01}$	6.01×10^{-02}	$1.58 \times 10^{+00}$
1.500	$7.66 \times 10^{+04}$	$8.08 \times 10^{+04}$	$8.56 \times 10^{+04}$	$1.130 \times 10^{+01}$	5.63×10^{-02}	$3.99 \times 10^{+00}$
1.750	$1.50 \times 10^{+05}$	$1.58 \times 10^{+05}$	$1.67 \times 10^{+05}$	$1.197 \times 10^{+01}$	5.42×10^{-02}	$6.14 \times 10^{+00}$
2.000	$2.58 \times 10^{+05}$	$2.71 \times 10^{+05}$	$2.86 \times 10^{+05}$	$1.251 \times 10^{+01}$	5.29×10^{-02}	$6.22 \times 10^{+00}$
2.500	$5.76 \times 10^{+05}$	$6.05 \times 10^{+05}$	$6.37 \times 10^{+05}$	$1.331 \times 10^{+01}$	5.10×10^{-02}	$3.90 \times 10^{+00}$
3.000	$1.01 \times 10^{+06}$	$1.06 \times 10^{+06}$	$1.12 \times 10^{+06}$	$1.388 \times 10^{+01}$	5.01×10^{-02}	$2.50 \times 10^{+00}$
3.500	$1.53 \times 10^{+06}$	$1.61 \times 10^{+06}$	$1.69 \times 10^{+06}$	$1.429 \times 10^{+01}$	5.03×10^{-02}	$2.15 \times 10^{+00}$
4.000	$2.09 \times 10^{+06}$	$2.20 \times 10^{+06}$	$2.32 \times 10^{+06}$	$1.461 \times 10^{+01}$	5.13×10^{-02}	$2.29 \times 10^{+00}$
5.000	$3.24 \times 10^{+06}$	$3.42 \times 10^{+06}$	$3.62 \times 10^{+06}$	$1.505 \times 10^{+01}$	5.48×10^{-02}	$2.54 \times 10^{+00}$
6.000	$4.29 \times 10^{+06}$	$4.54 \times 10^{+06}$	$4.82 \times 10^{+06}$	$1.533 \times 10^{+01}$	5.89×10^{-02}	$2.85 \times 10^{+00}$
7.000	$5.16 \times 10^{+06}$	$5.48 \times 10^{+06}$	$5.84 \times 10^{+06}$	$1.552 \times 10^{+01}$	6.28×10^{-02}	$3.23 \times 10^{+00}$
8.000	$5.84 \times 10^{+06}$	$6.22 \times 10^{+06}$	$6.65 \times 10^{+06}$	$1.564 \times 10^{+01}$	6.62×10^{-02}	$3.59 \times 10^{+00}$
9.000	$6.34 \times 10^{+06}$	$6.77 \times 10^{+06}$	$7.26 \times 10^{+06}$	$1.573 \times 10^{+01}$	6.90×10^{-02}	$3.92 \times 10^{+00}$
10.000	$6.70 \times 10^{+06}$	$7.17 \times 10^{+06}$	$7.71 \times 10^{+06}$	$1.579 \times 10^{+01}$	7.14×10^{-02}	$4.20 \times 10^{+00}$

- [1] R. Gratton, C. Sneden, and E. Carretta, *Annu. Rev. Astron. Astr.* **42**, 385 (2004).
- [2] R. G. Gratton, C. Sneden, and E. Carretta, *Astron. Astrophys.* **369**, 87 (2001).
- [3] P. Ventura, F. D'Antona, I. Mazzitelli, and R. Gratton, *Astrophys. J. Lett.* **550**, L65 (2001).
- [4] F. D'Antona, V. Caloi, J. Montalbán, P. Ventura, and R. Gratton, *Astron. Astrophys.* **395**, 69 (2002).
- [5] P. Denissenkov and F. Herwig, *Astrophys. J. Lett.* **590**, L99 (2003).
- [6] T. Decressin and C. Charbonnel, in *IAU Symposium: From Lithium to Uranium: Elemental Tracers of Early Cosmic Evolution*, edited by V. Hill, P. François, and F. Primas, Vol. S228 (Cambridge University Press, Cambridge, 2005), p. 395.
- [7] N. Prantzos and C. Charbonnel, *Astron. Astrophys.* **458**, 135 (2006).
- [8] T. Decressin, G. Meynet, C. Charbonnel, N. Prantzos, and S. Ekström, *Astron. Astrophys.* **464**, 1029 (2007).
- [9] S. de Mink, O. R. Pols, N. Langer, and R. G. Izzard, *Astron. Astrophys. Lett.* **507**, 1 (2009).
- [10] F. D'Antona and P. Ventura, *Mon. Not. R. Astron. Soc.* **379**, 1431 (2007).
- [11] J.-W. Lee, *Mon. Not. R. Astron. Soc.* **405**, L36 (2010).
- [12] C. Rowland, C. Iliadis, A. E. Champagne, C. Fox, J. José, and R. Runkle, *Astrophys. J.* **615**, L37 (2004).
- [13] G. Audi, A. H. Wapstra, and C. Thibault, *Nucl. Phys. A* **729**, 337 (2003).
- [14] P. M. Endt, *Nucl. Phys. A* **521**, 1 (1990).
- [15] S. E. Hale, A. E. Champagne, C. Iliadis, V. Y. Hansper, D. C. Powell, and J. C. Blackmon, *Phys. Rev. C* **70**, 045802 (2004).
- [16] J. Zyskind, M. Rios, and C. Rolfs, *Astrophys. J.* **243**, L53 (1981).
- [17] J. Goerres, M. Wiescher, and C. Rolfs, *Astrophys. J.* **343**, 365 (1989).
- [18] C. Iliadis, R. Longland, A. E. Champagne, A. Coc, and R. Fitzgerald, *Nucl. Phys. A* **841**, 31 (2010).
- [19] R. Longland, C. Iliadis, A. Champagne, J. Newton, C. Ugalde, A. Coc, and R. Fitzgerald, *Nucl. Phys. A* **841**, 1 (2010).
- [20] J. M. Cesaratto, A. E. Champagne, T. B. Clegg, M. Q. Buckner, R. Runkle, and A. Stefan, *Nucl. Instrum. Methods A* **623**, 888 (2010).
- [21] H. W. Becker, M. Bahr, M. Berheide, M. Buschmann, C. Rolfs, G. Roters, S. Schmidt, W. H. Schulte, G. E. Mitchell, and J. S. Schweitzer, *Z. Phys. A* **351**, 453 (1995).
- [22] S. Seuthe, H. W. Becker, A. Krauss, A. Redder, C. Rolfs, U. Schröder, H. P. Trautvetter, K. Wolke, S. Wüstenbecker, R. W. Kavanagh, and F. B. Waanders, *Nucl. Instrum. Methods A* **260**, 33 (1987).
- [23] J. M. Cesaratto, Ph.D. thesis, University of North Carolina at Chapel Hill, 2011.
- [24] D. Vermilyea, *Acta. Metall. Mater.* **1**, 282 (1953).
- [25] B. M. Paine and D. G. Sargood, *Nucl. Phys. A* **331**, 389 (1979).
- [26] P. W. M. Glaudemans and P. M. Endt, *Nucl. Phys.* **42**, 367 (1963).
- [27] A. D. Martin, K. M. Quinn, and J. H. Park, *J. Stat. Software* **42**, 22 (2011).
- [28] C. Iliadis, *Nuclear Physics of Stars* (Wiley-VCH, Weinheim, 2007).
- [29] R. Longland, C. Iliadis, A. E. Champagne, C. Fox, and J. R. Newton, *Nucl. Instrum. Methods A* **566**, 452 (2006).
- [30] S. Carson, C. Iliadis, J. Cesaratto, A. Champagne, L. Downen, M. Ivanovic, J. Kelley, R. Longland, J. R. Newton, G. Rusev, and A. P. Tonchev, *Nucl. Instrum. Methods A* **618**, 190 (2010).
- [31] I. J. Kim, C. S. Park, and H. D. Choi, *Appl. Radiat. Isotopes* **58**, 227 (2003).
- [32] S. Agostinelli *et al.*, *Nucl. Instrum. Methods A* **506**, 250 (2003).
- [33] M. Q. Buckner, C. Iliadis, J. M. Cesaratto, C. Howard, T. B. Clegg, A. E. Champagne, and S. Daigle, *Phys. Rev. C* **86**, 065804 (2012).
- [34] R. B. Firestone, *Nucl. Data Sheets* **108**, 2319 (2007).
- [35] Y. Zhu, *Nucl. Instrum. Methods A* **578**, 322 (2007).
- [36] R. D. Cousins, *Am. J. Phys.* **63**, 398 (1995).
- [37] C. Angulo, M. Arnould, M. Rayet, P. Descouvemont, D. Baye, C. Leclercq-Willain, A. Coc, S. Barhoumi, P. Aguer, C. Rolfs *et al.*, *Nucl. Phys. A* **656**, 3 (1999).
- [38] W. J. Vermehr, D. M. Pringle, and I. F. Wright, *Nucl. Phys. A* **485**, 380 (1988).
- [39] P. Ventura and F. D'Antona, *Astron. Astrophys.* **431**, 279 (2005).
- [40] P. Ventura (private communication, 2013).
- [41] A. L. Salaska, C. Iliadis, A. E. Champagne, S. Goriely, S. Starrfield, and F. X. Timmes, *Astrophys. J. Supp.* **207**, 18 (2013).
- [42] R. Longland, *Astron. Astrophys.* **548**, A30 (2012).